White Rose Research Online

eprints@whiterose.ac.uk
https://eprints.whiterose.ac.uk
Universities of Leeds, Sheffield and York

Deposited via The University of Sheffield.

White Rose Research Online URL for this paper:
https://eprints.whiterose.ac.uk/id/eprint/233758/

Version: Published Version

Article:
Germanis, S., Chen, X., Dost, R. et al. (2025) Waveguide excitation and spin pumping of chirally coupled quantum dots. Optica, 12 (10). pp. 1689-1696. ISSN: 2334-2536

https://doi.org/10.1364/optica.569882

Reuse
This article is distributed under the terms of the Creative Commons Attribution (CC BY) licence. This licence allows you to distribute, remix, tweak, and build upon the work, even commercially, as long as you credit the authors for the original work. More information and the full terms of the licence here:
https://creativecommons.org/licenses/

Takedown
If you consider content in White Rose Research Online to be in breach of UK law, please notify us by emailing eprints@whiterose.ac.uk including the URL of the record and the reason for the withdrawal request.

UNIVERSITY OF LEEDS
University of Sheffield
UNIVERSITY of York

Research Article Vol. 12, No. 10 / October 2025 / Optica 1689

Waveguide excitation and spin pumping of chirally coupled quantum dots

Savvas Germanis,[1,†] Xuchao Chen,[1,†] René Dost,[1] Dominic J. Hallett,[1] Edmund Clarke,[2] Pallavi K. Patil,[2] Maurice S. Skolnick,[1] Luke R. Wilson,[1] Hamidreza Siampour,[3,*] and A. Mark Fox[1,4]

[1]School of Mathematical and Physical Sciences, University of Sheffield, Hicks Building, Sheffield S3 7RH, UK
[2]EPSRC National Epitaxy Facility, School of Electrical and Electronic Engineering, University of Sheffield, Sheffield S1 3JD, UK
[3]School of Mathematics and Physics, Queen's University Belfast, University Road, Belfast BT7 1NN, UK
[4]mark.fox@sheffield.ac.uk
[†]These authors contributed equally to this work.
*h.siampour@qub.ac.uk

Received 5 June 2025; revised 25 September 2025; accepted 3 October 2025; published 17 October 2025

On-chip excitation of single quantum emitters is a key requirement for developing scalable quantum photonic technologies. Here, we report a remote excitation protocol on an integrated semiconductor chip, in which a single quantum dot (QD) is driven in-plane via a photonic-crystal waveguide through a *p*-shell optical transition. The chirality of the waveguide mode is exploited to achieve both directional absorption and directional emission, resulting in a substantial enhancement in directional contrast, as measured for the Zeeman components of the waveguide-coupled QD. This remote excitation scheme enables near-unity directionality (≥ 0.95) across ∼56% of the waveguide area, with significant overlap with the Purcell-enhanced region, where the electric field intensity profile is near its peak. In contrast, conventional out-of-plane local excitation yields only ∼25% overlap. This enhancement increases the likelihood of locating Purcell-enhanced QDs in regions that support high directionality, allowing the experimental demonstration of a six-fold enhancement in the decay rate of a QD with directionality of $90 \pm 3\%$. The remote p-shell excitation protocol thus establishes a benchmark for waveguide quantum optics by combining Purcell enhancement with high directionality. This approach enables efficient on-chip spin initialization and control in solid-state quantum technologies operating in high-β-factor regimes, with implications for scalable quantum networks and integrated devices.

Published by Optica Publishing Group under the terms of the Creative Commons Attribution 4.0 License. Further distribution of this work must maintain attribution to the author(s) and the published article's title, journal citation, and DOI.

https://doi.org/10.1364/OPTICA.569882

1. INTRODUCTION

The rapid evolution of photonic quantum technologies is driven by potential breakthroughs in quantum computing, communication, and sensing [1–3]. Central to this progress is the development of chip-scale quantum optical circuits that seamlessly integrate the excitation, manipulation, and detection of single photons [4–10]. A key component of this integration is on-chip excitation, where quantum emitters are excited via waveguide modes rather than using an off-chip laser. This technique is essential for implementing precise quantum operations, miniaturizing devices, and enabling more compact quantum technologies [5,11]. For instance, recent advancements in quantum sensing and light guiding, such as the use of fluorescent nanodiamond-doped polyvinyl alcohol (PVA) fibres, demonstrate promising applications in on-chip excitation [12]. This method offers several advantages, including reduced optical crosstalk, minimized local heating, the ability to excite multiple emitters using a single mode, and access to emitters in hard-to-reach regions of a photonic device. Additionally, this technique can be extended to chiral quantum systems, where engineering and preserving the polarization and flow of light within the waveguide allow information stored in polarized states to be transmitted unidirectionally [13]. This property is particularly advantageous for implementing directional quantum networks and distributed quantum computing architectures, where controlling the flow of quantum information is essential. Such chiral platforms not only enable spin-dependent routing of single photons but also enhance photon-mediated interactions between spatially separated emitters [14]. This capability is expected to play a central role in future quantum devices, where efficient interfacing between stationary qubits and flying photonic qubits is required for scalable architectures. Ultimately, integrating these elements into a unified, chip-scale platform will be key to realizing compact and robust quantum systems for real-world applications.

A key parameter for waveguide quantum optics is the β-factor, which quantifies the probability that an emitted or scattered photon is coupled to the waveguide mode. Values of the β-factor close to unity are required to observe strong quantum-optical

effects such as single-photon nonlinearities, and the high-β regime acquires additional interest when the quantum emitter is positioned at a chiral point of the waveguide [13]. For such a chirally coupled quantum emitter, a spin-dependent phase shift of π can be imparted to a photon propagating in a specific direction, and this can be exploited to develop quantum spin-networks [15]. There have been numerous observations of chiral emission from quantum emitters in a variety of nano-photonic systems [16–24], and in a recent paper, we demonstrated a notable combination of chiral emission with a high Purcell factor, and hence β-factor [25]. Furthermore, a hybrid cavity–waveguide device demonstrated electrically tunable, spin-dependent directional emission from quantum dots, achieving strong Purcell enhancement alongside near-unity directional contrast [26]. The underlying mechanism in that work relies on cavity–waveguide interference, which differs from the waveguide-only approach pursued here. While cavity systems achieve impressive directionality and Purcell factors, optimal coupling is confined to one or a few spatial points within the cavity field. In contrast, waveguide-based designs support an extended "spatial chiral area," where emitters simultaneously experience high Purcell factor, high β-factor, and significant directionality, providing a more scalable platform for multi-emitter integration in quantum networks.

However, the demonstration of directional absorption associated with the chirality of the waveguide modes has received far less attention, with all previous studies restricted to nanobeam waveguides in regimes of only moderate β-factor [11,27,28]. The in-plane excitation geometry permits efficient spin pumping via a remote laser of arbitrary polarization [11] and establishes protocols for spin-dependent dot-to-dot interactions in a chip-based geometry. This capability is crucial for developing spin-based quantum computing architectures and advancing quantum communication technologies. Furthermore, it enables the interaction of quantum spin states from two or more QDs within photonic devices, mediated through photons, which is essential for the implementation of spin cluster states [15,29,30].

In this work, we push the boundaries of in-plane excitation by exploiting the chirality of slow-light waveguide modes to initialize exciton spins in the high β-factor regime. We employ a remote excitation method that significantly enhances the directional contrast under a linearly-polarized pump. Specifically, we demonstrate that, when combined with glide-plane photonic crystal waveguides, in-plane p-shell excitation enables the efficient initialization of circularly polarized spin states, leading to enhanced directionality of the emitted photons. These photons are coupled to the right- or left-circularly polarized propagating waveguide mode, depending on their polarization. This approach not only improves the directionality of emitter-waveguide interactions but also facilitates the coherent manipulation and readout of quantum information encoded in these spins. Our method introduces a novel protocol that leverages both p-shell excitation and slow-light enhancement to achieve a unique combination of directional absorption and directional emission with near-unity coupling efficiency (β-factor). A particularly impactful aspect of this approach is the elimination of off-chip pump lasers for excitation, which represents an important step toward large-scale, fully integrated quantum photonic architectures. By utilizing propagating waveguide modes for both excitation and spin initialization, the system significantly simplifies the design of quantum light sources and enables on-chip control over individual quantum emitters—a critical requirement for scalable quantum information processing. Furthermore, this protocol fully exploits the polarization content of the waveguide modes, offering a versatile and efficient mechanism for the initialization of emitter spin states, which is essential for advancing chip-based quantum technologies. In addition to efficient spin initialization, the slow-light regime enhances light–matter interactions and promotes collective effects such as superradiance through dot-to-dot coupling [13], further boosting the performance and coherence of quantum photonic systems.

2. REMOTE EXCITATION METHOD

Figure 1 illustrates the device layout and working principle. The device consists of a glide-plane photonic-crystal waveguide containing quantum dots with in- and out-couplers at opposite ends, as illustrated in Fig. 1(a). The quantum dots are located within a p–i–n diode as shown in Fig. 1(b) to enable exciton tuning via the quantum-confined Stark effect. This tunability is particularly important for photonic-crystal waveguides in which slow-light enhancement is only achieved at specific wavelengths. On application of a strong external magnetic field in Faraday geometry, the QD exciton states are circularly polarized, with the Zeeman components having opposite helicities. If the quantum dot is located at a chiral point of the waveguide, the modes are circularly polarized [see inset to Fig. 1(a)], with the helicity depending on the direction of propagation. Hence photons with opposite circular polarizations generated by exciton recombination propagate to either left or right according to their helicity. The Zeeman lines are therefore observed with differing intensities at the out-couplers, with their intensity ratio depending on the relative populations of the exciton spin states and on the chirality of the waveguide.

Figures 1(c) and 1(d) contrast two possible methods to excite the quantum dot, namely local and remote. In local excitation, the QD is directly pumped by an external laser field, as shown in Fig. 1(c). This is the method employed in the great majority of previous studies [16–18,25]. If the excitation is resonant or near-resonant with linearly polarized or unpolarized light, both exciton spin states (σ^+ and σ^-) are populated equally. A similar balance is expected for non-resonant pumping with any polarization due to the lack of spin memory. Under these conditions, the intensity ratio of the Zeeman components reflects only the local chirality of the waveguide mode at the QD position.

Figure 1(d) illustrates the contrasting case of the remote excitation scheme, where the laser is focused on one of the grating couplers at the end of the device and the quantum dot is excited via photons propagating within the waveguide. In this case, a quantum dot at a chiral point will be driven by a circularly polarized field irrespective of the polarization of the pump laser, with the helicity of the circular field depending on the direction of propagation. As a result, the waveguide effectively acts as a polarization filter: only the exciton spin state that couples to the chosen propagation direction is excited. This provides a simple intuitive distinction from local excitation, where both spin states may be populated and the observed contrast depends sensitively on relaxation dynamics. In our experiment, the system was initialized by pumping at a quasi-resonant energy, which can be attributed to a resonance (see Figure S2 in Supplement 1) within the p-shell [11,31,32]. This pumping scheme enables robust spin-state initialization and removes the need for additional optical filtering to distinguish between resonant laser light and photons emitted by the QD, which is non-trivial in planar devices [33,34]. The photogenerated

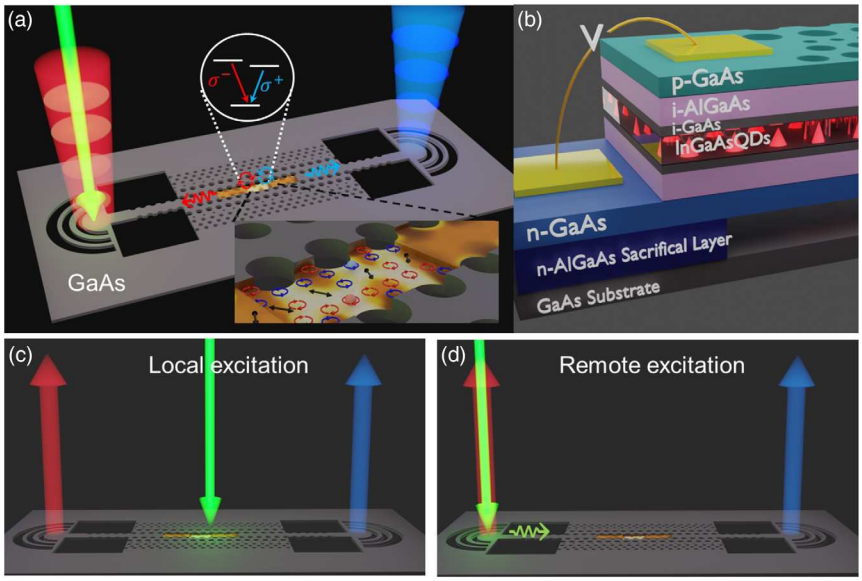

Fig. 1. Schematic of the device layout and working principle. (a) A semiconductor chip where a pump laser, indicated by a green arrow, is coupled into a waveguide using a grating. The waveguide directs light toward a QD positioned within the chiral region of the waveguide. The helicity of the waveguide mode in the photonic-crystal line defect enables selective excitation of the QD spins. Once excited, photons emitted from the QD couple to the waveguide mode and propagate either to the left (red) or right (blue) along the waveguide, depending on their circular polarization. The inset shows the intensity profile and helicity (chirality) of the waveguide mode within the slow-light section of the photonic-crystal line defect. (b) Schematic of the p–i–n GaAs diode structure with embedded InGaAs QDs and electrical contacts (yellow) made to the p- and n-GaAs layers. (c) Schematic of the local excitation scheme, where the pump laser is focused directly onto the QD. (d) Schematic of the remote excitation scheme, where the QD is excited via waveguide modes.

carriers in the excited state subsequently relax non-radiatively to the s-shell, preserving the spin memory of their initial state [35–37]. The precise nature of the excited state does not affect our argument, provided it preserves spin on relaxation to the s-shell. The s-shell excitons primarily recombine radiatively, emitting circularly polarized photons into the waveguide. Photons of different helicities then propagate in opposite directions according to the chirality at the QD's position.

The chief difference between the two excitation methods is that the chirality of the waveguide enters twice into the intensity ratio of the Zeeman components for the remote excitation method. First, the initial populations of the σ^+ and σ^- excitons are determined by the helical pumping at the chiral point, and hence are not the same. Second, the directional emission of the opposite spin states is again determined by the chirality. These two effects combine to produce a much stronger directional contrast between the Zeeman components for remote excitation compared to local excitation, where the chirality only affects the results at the second stage. While a similar directional contrast can be achieved using circularly polarized local excitation, this approach requires additional off-chip optical components and polarization control of the excitation laser [38] (see Supplement 1, Figure S3). In contrast, our method offers clear advantages in terms of on-chip integrability, simplicity of implementation, and emission efficiency. These attributes are crucial for the development of scalable quantum photonic circuits, where precise and efficient control over individual emitters must be achieved within a compact, integrated platform. The successful observation of enhanced directionality for remote excitation thus establishes the effectiveness of the chiral spin-pumping method, and hence demonstrates the validity of photon-mediated spin–spin interaction in chip-based photonic circuits.

3. NUMERICAL SIMULATIONS

Figure 2(a) shows the simulated chirality map of the glide-plane photonic crystal waveguide used in the device's slow-light region. The map is calculated using the Stokes parameters, S_3 and S_0, to visualize the degree of circular polarization, represented as $C_l = S_3/S_0$. Here $S_3 = -2\mathrm{Im}(E_x E_y^*)$, where E_x and E_y are the electric field components within the sample plane, and $S_0 = I$ is the light intensity. The subscript l in C_l indicates that this is the chirality measured using the local excitation method according to the position of the quantum emitter. The map shows strong chirality, with $C_l \geq 0.95$ in certain regions (solid black contour), enabling efficient coupling between exciton spins and the waveguide modes, thus facilitating controlled spin initialization and manipulation. The waveguide's band structure reveals two bands [Fig. 2(b)], with the simulated Purcell factor shown near the crossing point (i.e., $ka/\pi = 0.44$), where the slow-light effect is most pronounced. The spatial dependence of the chirality and the Purcell factor demonstrates that regions of strong chirality and high Purcell factor coincide. Restricting chirality to $C_l \geq 0.95$ (solid black contour), the overlap region covers more than 25% of the waveguide area, and includes areas with a predicted Purcell factor exceeding 20.

The helicity of the waveguide mode in the photonic-crystal line defect allows for the selective excitation of QD spins via remote excitation followed by directional absorption [Fig. 1(d)], as opposed to local excitation [Fig. 1(d)]. We consider a few-level quantum system corresponding to either a neutral exciton (X°) or a charged exciton (X^+/X^-), where the bracket notation denotes the energy level and spin handedness (e.g., $|g, +\rangle$ for a ground-state charged QD supporting a σ^+ transition, or $|e, -\rangle$ for an s-shell exciton with a σ^- transition.) When photons from a CW laser propagate along the waveguide and drive a QD dipole

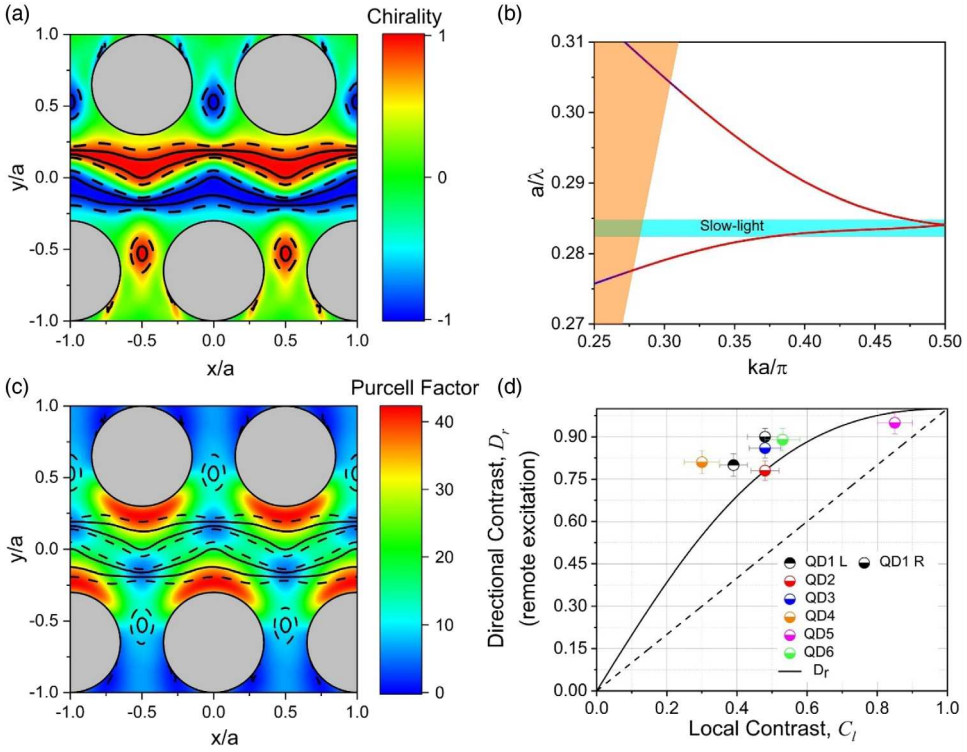

Fig. 2. (a) Simulated chiral map of the photonic-crystal waveguide slow-light region, showing regions of high local chirality ($C_l > 0.95$, solid black contour), calculated using Stokes parameters. These regions enable efficient coupling between QD spins and waveguide modes. Under remote excitation, the high directional contrast ($D_r \geq 0.95$) region covers ∼56% of the waveguide area (dashed black contour), compared to ∼25% for local excitation. (b) Band structure of the waveguide showing two bands, with the Purcell enhancement factor being most pronounced near the crossing point. The slow-light region is highlighted by the cyan stripe, indicating where group velocity is significantly reduced. (c) Simulated Purcell factor in the slow-light region. The solid and dashed contours show regions with directional contrast (≥ 0.95) under remote and local excitation, respectively, as in (a). The solid contour includes areas with Purcell factor >20, illustrating the efficiency of remote excitation in expanding the highly directional regions for QD spin control. (d) The relationship between directional contrast under remote excitation (D_r) and the local contrast (C_l) exhibits a substantial increase in effective directional contrast for measurements with remote excitation. The solid line is derived from the conversion formula given in Eq. (3), the dashed line shows $D_r = C_l$ relation, and the circles represent experimental data described in the next section.

transition, the polarization of the local electric field is transferred to the exciton. The resulting steady-state populations, $|\alpha_n|^2$ and $|\beta_n|^2$, reflect the local S_3 parameter of the waveguide mode. Here, $|\alpha_n|^2 = \langle e, +|\rho_{ss}|e, +\rangle$ and $|\beta_n|^2 = \langle e, -|\rho_{ss}|e, -\rangle$ represent the population coefficients of the two s-shell exciton spin states, with ρ_{ss} denoting the steady-state density matrix. Assuming identical radiative decay rates and dephasing for both spin components, the exciton spin populations directly determine the fraction of σ^+ and σ^- photons emitted from the QD. If $|\alpha_n|^2 \neq |\beta_n|^2$, the imbalance in the population of the two Zeeman states significantly affects the measured directional contrast, as the polarization-dependent absorption is followed by directional emission, and both processes depend on C_l. By contrast, for local excitation with linear polarization or in conditions where there is no spin memory, it follows that $|\alpha_n|^2 = |\beta_n|^2$, and the directionality just depends on the value of C_l for the emission process. Consequently, the directional contrast observed under in-plane remote excitation differs from that observed under local excitation with a linearly polarized pump.

To further analyze this effect, we derive a conversion formula that quantitatively relates the directionality observed through local excitation to that achieved under remote excitation. This relationship holds under the assumptions of the circular dipole approximation, spin-preserving scattering, and weak excitation. Specifically, consider a QD located where the intensity ratio between the Zeeman components collected from a single outcoupler under local excitation is ξ_e:1. The parameter ξ_e is defined as the ratio of emission rates between the σ^+ and σ^- transitions coupled into the propagating mode, and is determined by the Stokes parameters as $\xi_e = \left|\frac{1+S_3/S_0}{1-S_3/S_0}\right|$. The directional contrast in this scenario is given by

$$C_l = \left(\frac{|\alpha_n|^2}{|\beta_n|^2}\cdot\xi_e - 1\right) \Big/ \left(\frac{|\alpha_n|^2}{|\beta_n|^2}\cdot\xi_e + 1\right). \quad (1)$$

If we assume that the populations of the σ^+ and σ^- polarized exciton spin states are identical under local excitation (i.e., $|\alpha_n|^2 = |\beta_n|^2$), then C_l will be equal to the value of S_3/S_0 at the position of the quantum dot. This assumption is valid for a linearly polarized pump. It will also be valid for any pump polarization under conditions where the spin memory is lost after excitation. The relation between local and remote excitation contrast introduced here is intended only as a phenomenological guide. It captures the qualitative trend observed but does not provide a rigorous quantitative prediction. Several factors not included in the simple formulation, such as asymmetries in radiative decay, waveguide losses, back-reflection and scattering at the slow-to-fast light section, and finite fidelity of p-shell excitation, can all lead to deviations from the idealized curve (see Supplement 1, S7).

Under remote excitation, electron-hole pairs are generated with the exciton spin populations reflecting the polarization of the local electric field, resulting in a population ratio of $|\alpha_n|^2{:}|\beta_n|^2 = \xi_a{:}1$. Here, ξ_a denotes the ratio of total absorption rates between the σ^+ and σ^- transitions. In the ideal case of 100% spin fidelity, quantum spin information in the form of photon directionality is fully transferred to the polarization of excitons, such that ξ_a shares the same expression as ξ_e. Following excitation, the exciton emits σ^+ and σ^- photons with a relative intensity of $\xi_e{:}1$. These emitted photons are then coupled into the waveguide mode with polarization selectivity, introducing an additional factor of $\xi_e{:}1$ in the collection path. This spin-selective, directional excitation (absorption), followed by another directional emission process, leads to an intensity ratio of $\xi_a\xi_e{:}1$ for the collected signal. Assuming that $\xi_a = \xi_e$, the ratio under remote excitation ($\xi_e^2{:}1$) is therefore a square of that under local excitation ($\xi_e{:}1$). Consequently, the effective directional contrast under remote excitation, which reflects the combined effects of both directional absorption and directional emission, is given by

$$D_r = \left(\xi_e^2 - 1\right)/\left(\xi_e^2 + 1\right). \tag{2}$$

By substituting $\xi_e = (1 + C_l)/(1 - C_l)$, we obtain the following expression:

$$D_r = 2C_l/\left(1 + C_l^2\right). \tag{3}$$

This relationship reveals that the directional contrast under remote excitation depends on the initial contrast C_l but exhibits a non-linear enhancement for moderate values of C_l, as illustrated in Fig. 2(d). The graph in Fig. 2(d) shows a direct comparison between the theoretical model described by Eq. (3) and the experimental data points, which will be discussed further in the next section. This suggests that a modest directionality observed under direct excitation using a linearly polarized pump can yield a substantial increase in effective directional contrast for measurements with remote excitation.

For example, if $C_l = 0.5$ (corresponding to an intensity ratio of 3:1), the resulting effective directional contrast will reach $D_r = 0.8$—a significant improvement. Additionally, remote excitation can expand the effective area of directionality for waveguide-based photonic devices. In particular, the area with over 95% effective directional contrast increases from 25% to 56% in our glide-plane waveguide devices under remote excitation [dashed black contour in Fig. 2(a)]. This represents more than a twofold expansion of the highly directional region compared to local excitation, and the expanded region encompasses areas with strong Purcell enhancement exceeding 20 [solid black contour in Fig. 2(c)]. Our remote excitation technique takes advantage of the helicity of the slow-light waveguide mode, enabling the combination of higher Purcell factors and near-unity directional contrast. This balance underscores the potential of remote excitation in optimizing chiral photonic systems for waveguide quantum optics.

4. EXPERIMENTAL RESULTS

In the experiment, the sample is housed in a liquid helium cryostat surrounded by superconducting coils, enabling magneto-photoluminescence studies under an applied magnetic field along the sample axis (see setup in Supplement 1, Figure S1). For quasi-resonant excitation, the laser is tuned to energies just above the exciton state, specifically targeting the QD's p-shell. As shown in the photoluminescence (PL) excitation spectrum in Figure S2, the p-shell is located at ∼896 nm, approximately 20.7 meV (14 nm) above the exciton emission line at 910 nm.

We measured the PL of the exciton emission line under p-shell excitation while applying an external magnetic field of 3 T in the Faraday geometry. Directional contrast D is defined as $D = \frac{I_{\sigma+} - I_{\sigma-}}{I_{\sigma+} + I_{\sigma-}}$, where $I_{\sigma+}$ and $I_{\sigma-}$ are the integrated areas of the σ^+ and σ^- exciton lines measured from the same out-coupler. Using a single output port ensures that losses from waveguide reflections, out-couplers, propagation, and detection are effectively cancelled. The small spectral splitting (∼0.4 nm at 3 T) ensures that wavelength-dependent variations do not affect the measurement. This approach provides a robust measure of directional contrast while avoiding the need for full calibration of left- and right-propagating modes.

For the local excitation scheme [Fig. 1(c)], where the pump laser is focused directly on the QD1, the PL spectra [Fig. 3(a)] exhibit relatively weak directionality. In contrast, under the remote excitation scheme [Fig. 1(d)], where the QD1 is excited via waveguide modes, the PL spectra [Fig. 3(b)] show a significantly enhanced directional contrast. This enhancement is attributed to stronger spin-selective pumping of the QD via the waveguide mode, driven by directional absorption and, in turn, directional coupling of the QD emission within the glide-plane photonic-crystal devices.

In Fig. 2(d), we present data from a study of six QDs coupled into the glide-plane waveguide, represented by coloured points. The graph compares the directionality for remote excitation and local excitation, with the prediction of Eq. (3) for D_r shown by the solid line. The dashed line shows the case where there is no enhancement under remote excitation, i.e., $D_r = C_l$. For all QDs shown in this graph, excitation conditions were carefully selected to ensure p-shell excitation above the QD ground states. Black circular points correspond to the values from QD1, the primary QD studied in this report. The labels L and R indicate the two out-couplers where the PL was collected. The variation between points arises from chiral asymmetry, commonly observed in these devices due to waveguide disorder and multiple scattering processes affecting the propagating mode (see, e.g., Ref. [16]). Red, blue, orange, pink, and green circular points represent PL measurements from QDs in other devices with the same chiral design parameters. Most of these QDs, embedded within the glide-plane photonic-crystal waveguide, exhibit relatively low chiral behaviour under local excitation. In all cases, the directional contrast increases under remote excitation. It is striking that the enhancement is close to, or sometimes larger, than that predicted by Eq. (3), which confirms that the spin memory under p-shell excitation is close to 100%. For the data points lying above the prediction curve in Fig. 2(d), we identified two major mechanisms that could lead to systematic deviations. First, the polarization and mode profile of the waveguide mode at the p-shell excitation wavelength generally differ from those of the s-shell emission at the QD position (so $\xi_a \neq \xi_e$), which is most likely the case in our device. Second, although special attention was given to excitation of the p-shell resonance, small detuning of the pump laser could preferentially favour one transition (σ^+ or σ^-) over the other. Additional contributions may arise from breakdown of the point-dipole approximation [39,40], ellipticity of the dipole moment, pump beam ellipticity, and reflections at the slow-to-fast waveguide interface. All of these factors could drive the population imbalance away from the ideal case and shift the measured contrast between the two Zeeman components.

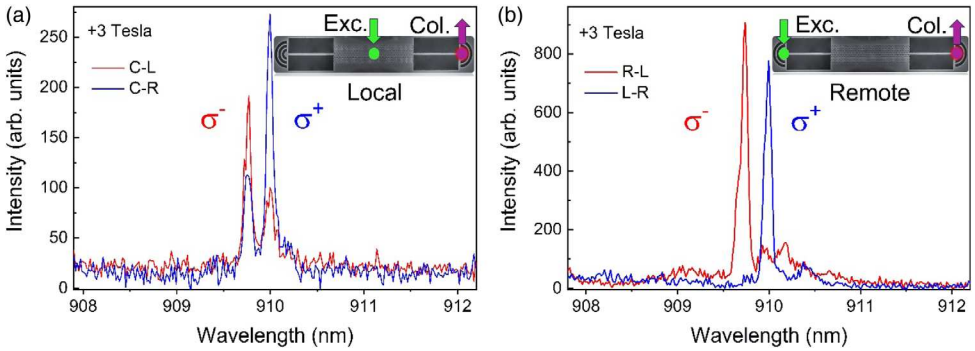

Fig. 3. PL spectra of the exciton emission line under an external magnetic field of 3 T in Faraday geometry where the field is applied along the sample growth axis. (a) PL spectra for local excitation and (b) corresponding PL spectra for remote excitation. The comparison highlights the significant enhancement in the directional emission under remote excitation, demonstrating improved spin-selective interactions.

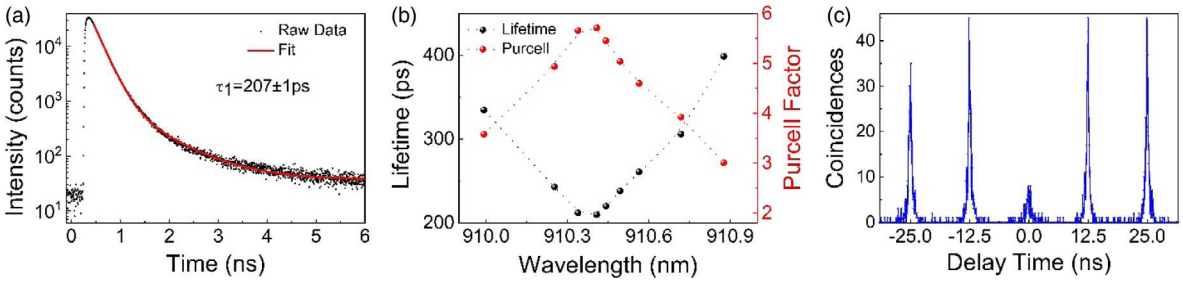

Fig. 4. Emission characteristics and single-photon verification of the QD. (a) Lifetime measurement of the QD at a wavelength of 910.4 nm, demonstrating a lifetime of approximately 200 ps and a six-fold enhancement in the decay rate compared to the ensemble lifetime of 1.2 ns. (b) Wavelength dependence of the QD's lifetime and corresponding Purcell factor as the wavelength is tuned by electric field within the slow light region. It shows a decrease in decay time as the emission wavelength nears the center of the slow-light band, followed by an increase as the wavelength moves past the center. (c) Auto-correlation PL histograms, without background correction, were obtained through HBT correlation measurements on the exciton line.

Figures 4(a) and 4(b) show time-resolved PL measurements to assess the decay rate enhancement in the slow-light waveguide for the same QD1 as in Fig. 3. In our experiments, electrical and magnetic field tuning were generally employed to achieve a red or blue shift, resulting from either or both the quantum-confined Stark effect and the Zeeman energy. Specifically, for QD1, electrical field tuning was applied at zero magnetic field to induce a red shift and align the QD's wavelength as closely as possible with the centre of the slow-light band of the photonic-crystal waveguide (Supplement 1, Figure S5). Figure 4(a) shows the time-resolved PL at a wavelength of 910.4 nm, where the emission is the fastest. In addition, Fig. 4(b) shows the variation in lifetime with emission wavelength as the electric field is increased and red-shift tuning is applied. It demonstrates a reduction in decay time within the slow-light band as the emission wavelength approaches the centre of the band, followed by an increase in decay time as the wavelength moves beyond the centre, returning to larger values. The wavelength dependence of the simulated Purcell factor, confirming the spectral alignment between enhanced emission and slow-light regions of the waveguide, is presented in Supplement 1, Section S5. For the time-resolved PL measurements in the remote excitation scheme, the excitation energy was tuned to maintain a constant detuning of 20.7 meV from the exciton emission energy. The decay is best described by a bi-exponential function: $I = I_0 + Ae^{\frac{-|t-t0|}{\tau_1}} + Be^{\frac{-|t-t_0|}{\tau_2}}$, with $t_0 = 459$ ps as the fit starting point and $I_0 = 37.1 \pm 2.1$ as a free offset parameter. The dominant fast decay component has $\tau_1 = 207 \pm 1$ ps with amplitude $A = 24.1$, corresponding to exciton recombination following rapid relaxation from the nearest p-shell resonance (20.7 meV detuning). A weaker slow component with $\tau_2 = 802 \pm 36$ ps and amplitude $B = 1.2$ is attributed to relaxation via higher states excited by the broadband femtosecond pulses, or to weak emission from neighbouring QDs within the 0.5 nm collection window. The raw decay is plotted on a logarithmic scale in Fig. 4(a) to highlight both fast and slow decay components. The bi-exponential fit in Fig. 4(a) indicates a lifetime of approximately 200 ps, corresponding to a six-fold decay rate enhancement compared to the ensemble lifetime of 1.2 ns for the dots in the wafer. This results in an estimated Purcell factor of 6 for the chirally coupled QD1, achieving a significant combination of high directional contrast ($90 \pm 3\%$) and Purcell factor in a QD, and demonstrating spin pumping of the QD1 in the slow-light region of glide-plane waveguides where the estimated β-factor, calculated using FDTD simulations, is 97%. A benchmarking comparison of our device against other representative chiral quantum optical waveguide platforms—including nanobeams, photonic crystal waveguides, and topological waveguides—is presented in Supplement 1, Section S6 (Table S1), highlighting the competitive performance of our approach as regards chiral area, Purcell factor, and β-factor.

Figure 4(c) shows Hanbury Brown–Twiss (HBT) measurements of the second-order correlation function $g^2(\tau)$ under pulsed excitation at the p-shell absorption line, operating below the saturation regime of the exciton state. The multiphoton emission at zero delay is strongly suppressed, demonstrating the quantum dot's capability as a reliable single-photon source. Pulsed-excitation $g^2(\tau)$ was obtained directly from the raw coincidence counts by integrating a fixed 2 ns window for each peak and calculating the

ratio of the $\tau = 0$ peak to the mean of the adjacent peaks, resulting in $g^2(0) = 0.26$. This value is higher than that observed under continuous-wave (CW) excitation, as shown in Figure S4. The femtosecond laser was centred on the p-shell resonance but was not spectrally shaped. The broadband pulse width may allow weak excitation of higher-lying states, which could contribute a small background signal and reduce the single-photon purity compared with CW excitation. We observe strong photon antibunching behaviour in both CW and pulsed excitation schemes, confirming that this quantum dot is a viable single-photon source for chiral quantum-optical experiments. For the pulsed excitation measurements, we stabilized the charge environment using a weak above-band 808 nm laser with a power of ∼3 nW, nearly three orders of magnitude lower than the 1 μW p-shell excitation. This very low power ensures negligible perturbation of the system while suppressing charge fluctuations and reducing spectral wandering of the exciton emission line. The charge noise in our devices is attributed to the thick AlGaAs barriers enclosing the QD layer and to oxide-related surface states. A weak above-band stabilization laser was therefore applied, consistent with earlier reports [33,41,42]. In its absence, the exciton line exhibited intensity and energy fluctuations on the order of one second. This approach significantly improved the signal quality, particularly for the lifetime measurements. The HBT results under CW excitation are provided in Supplement 1 (Figure S4).

5. METHODS

A. Photoluminescence Measurements

Measurements were performed in a helium bath cryostat (Supplement 1, Figure S1) at T = 4 K equipped with a superconducting magnet (0–5 Tesla). The sample was mounted in a socket giving access to electrical control of the PIN devices. The sample holder apparatus was fixed on a X-Y-Z piezo-stage, ensuring stable positioning of the sample. The optical access of the sample was through a confocal scanning microscope setup. A CW tunable laser (Toptica single-mode laser DL Pro) was used for PL excitation and p-shell excitation experiments, while a femtosecond pulsed Ti:Sapphire laser (Spectra-Physics Tsunami, Newport) with an 80 MHz repetition rate was used for lifetime and PL correlation experiments. Both lasers were fibre-coupled. On the collection path, an ultranarrow bandpass filter with a full width at half-maximum (FWHM) of less than 0.55 nm (935.4–0.45 OD5 Ultra Narrow Bandpass Filter, Alluxa) was angle-tuned with respect to the emission line of the QD under study, effectively filtering out unwanted emission lines and the quasi-resonant p-shell excitation laser from the QD signal. PL spectra were recorded by a liquid nitrogen-cooled charge-coupled device (CCD) camera after being dispersed through a 0.75 Acton Pro monochromator. Time-resolved PL measurements were implemented by using superconducting nanowire fast single-photon detectors (SNSPD—Single Quantum Eos), while the laser pulse repetition rate was detected by a photodiode. The pulses from the SNSPD and the photodiode were analyzed using a time-correlated photon counting card (Becker and Hickl SPC-130-EM).

B. Simulation

Numerical calculations were performed using the commercial software package Lumerical FDTD Solutions and the open-source Python package Legume (see details in Supplement 1, Section 3).

C. Diode Structure

The p–i–n GaAs diode structure follows the design used in our previous work [25].

6. DISCUSSION AND CONCLUSION

By demonstrating enhanced directional contrast through remote excitation and combining it with Purcell enhancement, we introduce a novel mechanism for improving chiral light–matter interactions in nanophotonic platforms in the high-β regime that is required for waveguide quantum optics. The process of spin-photon coupling plays a critical role, that is, the transfer of photon polarization to the exciton spin, followed by its recombination and subsequent re-emission. The method only works when the exciton spin is preserved during relaxation, as any decoherence processes would lower the final chiral response, which is why we use p-shell excitation. Alternative schemes for driving s-shell excitons while preserving spin include phonon-assisted excitation [43], and the multi-pulse "swing-up" method [44]. Our photonic device can support these approaches, highlighting its versatility for integrated quantum photonics. In our work, we have focused on exciton spins, but the method can easily be adapted for spin pumping of electrons and holes in charged quantum dots, opening up new possibilities for spin-based quantum networks and quantum information processing systems.

Our investigation demonstrates the potential of remote excitation techniques combined with photonic-crystal waveguides to significantly enhance spin initialization and directional coupling of QDs. By leveraging the chirality of waveguide modes in the slow-light regime, we have expanded the region of high directionality, theoretically achieving directionality exceeding 95% and a Purcell enhancement greater than 20. The simulations highlight a substantial improvement when using remote excitation, with approximately 56% of the waveguide area having ≥ 95% directionality—compared to only around 25% achieved with local excitation methods. Furthermore, our experimental measurements demonstrate a six-fold enhancement in the emission decay rate of a coupled QD with 90 ± 3% directional contrast under remote excitation, which corresponds to a β-factor of ∼97%, as calculated using FDTD simulations. This advancement enables improved control of quantum states and facilitates the integration of such systems into chip-scale quantum optical circuits. This work provides a foundation for future research to optimize chiral quantum emitter interactions within photonic circuits, an important step toward functional quantum devices. While no pre-selection of QD position was applied in the present devices, future work will focus on the integration of deterministic QD positioning techniques. Combining such site-controlled growth or post-fabrication tuning with the demonstrated remote excitation protocol could further optimize the overlap with both the high-Purcell and high-directionality regions, and strengthen the scalability of chiral quantum photonic architectures.

Funding. Engineering and Physical Sciences Research Council (EP/V026496/1); UK Research and Innovation (Smart Nano NI).

Acknowledgment. Hamidreza Siampour acknowledges support from the UKRI Strength in Places Fund programme, Smart Nano NI, and technical assistance from Shelby Hanna in creating Fig. 1. Savvas Germanis and Xuchao Chen performed the measurements. Hamidreza Siampour designed the photonic devices, and René Dost conducted the device fabrication. Edmund Clarke and Pallavi K. Patil grew the quantum dot wafer. Xuchao Chen contributed to the simulations. Hamidreza Siampour and A. Mark Fox supervised the experiment. Hamidreza Siampour wrote the paper with input from Savvas Germanis and Xuchao Chen. All authors discussed the results and commented on the paper.

Disclosures. The authors declare no conflicts of interest.

Data availability. The data that support the findings of this study are available from the authors.

Supplemental document. See Supplement 1 for supporting content.

REFERENCES

1. D. D. Awschalom, R. Hanson, J. Wrachtrup, *et al.*, "Quantum technologies with optically interfaced solid-state spins," Nat. Photonics **12**, 516–527 (2018).
2. E. Pelucchi, G. Fagas, I. Aharonovich, *et al.*, "The potential and global outlook of integrated photonics for quantum technologies," Nat. Rev. Phys. **4**, 194–208 (2022).
3. M. Atatüre, D. Englund, N. Vamivakas, *et al.*, "Material platforms for spin-based photonic quantum technologies," Nat. Rev. Mater. **3**, 38–51 (2018).
4. J. Wang, F. Sciarrino, A. Laing, *et al.*, "Integrated photonic quantum technologies," Nat. Photonics **14**, 273–284 (2020).
5. H. Siampour, S. Kumar, V. A. Davydov, *et al.*, "On-chip excitation of single germanium vacancies in nanodiamonds embedded in plasmonic waveguides," Light Sci. Appl. **7**, 61 (2018).
6. R. W. Heeres, L. P. Kouwenhoven, and V. Zwiller, "Quantum interference in plasmonic circuits," Nat. Nanotechnol. **8**, 719–722 (2013).
7. C. Wu, C. Ma, and Z. Wang, "Excitation, generation, positioning, and modulation for quantum light sources integrated on chip," in *Integrated Nanophotonics* (2023), pp. 135–165.
8. H. Siampour, S. Kumar, and S. I. Bozhevolnyi, "Chip-integrated plasmonic cavity-enhanced single nitrogen-vacancy center emission," Nanoscale **9**, 17902–17908 (2017).
9. A. Eich, T. C. Spiekermann, H. Gehring, *et al.*, "Single-photon emission from individual nanophotonic-integrated colloidal quantum dots," ACS Photonics **9**, 551–558 (2022).
10. P. P. J. Schrinner, J. Olthaus, D. E. Reiter, *et al.*, "Integration of diamond-based quantum emitters with nanophotonic circuits," Nano Lett. **20**, 8170–8177 (2020).
11. R. J. Coles, D. M. Price, B. Royall, *et al.*, "Path-dependent initialization of a single quantum dot exciton spin in a nanophotonic waveguide," Phys. Rev. B **95**, 121401 (2017).
12. R. Styles, A. Candini, V. Guarino, *et al.*, "Quantum sensing and light guiding with fluorescent nanodiamond-doped PVA fibers," Adv. Opt. Mater. **12**, 2302940 (2024).
13. P. Lodahl, S. Mahmoodian, S. Stobbe, *et al.*, "Chiral quantum optics," Nature **541**, 473–480 (2017).
14. S. Cardenas-Lopez, S. J. Masson, Z. Zager, *et al.*, "Many-body superradiance and dynamical mirror symmetry breaking in waveguide QED," Phys. Rev. Lett. **131**, 033605 (2023).
15. S. Mahmoodian, P. Lodahl, and A. S. Sørensen, "Quantum networks with chiral-light–matter interaction in waveguides," Phys. Rev. Lett. **117**, 240501 (2016).
16. R. J. Coles, D. M. Price, J. E. Dixon, *et al.*, "Chirality of nanophotonic waveguide with embedded quantum emitter for unidirectional spin transfer," Nat. Commun. **7**, 11183 (2016).
17. I. Söllner, S. Mahmoodian, S. L. Hansen, *et al.*, "Deterministic photon–emitter coupling in chiral photonic circuits," Nat. Nanotechnol. **10**, 775–778 (2015).
18. M. Mehrabad Jalali, A. P. Foster, R. Dost, *et al.*, "Chiral topological photonics with an embedded quantum emitter," Optica **7**, 1690–1696 (2020).
19. B. Lang, D. P. S. McCutcheon, E. Harbord, *et al.*, "Perfect Chirality with imperfect polarization," Phys. Rev. Lett. **128**, 073602 (2022).
20. N. V. Hauff, H. JeannicLe, P. Lodahl, *et al.*," Chiral quantum optics in broken-symmetry and topological photonic crystal waveguides," Phys. Rev. Res **4**, 023082 (2022).
21. N. J. Martin, M. Jalali Mehrabad, X. Chen, *et al.*, "Topological and conventional nanophotonic waveguides for directional integrated quantum optics," Phys. Rev. Res **6**, L022065 (2024).
22. I. J. Luxmoore, N. A. Wasley, A. J. Ramsay, *et al.*, "Interfacing spins in an InGaAs quantum dot to a semiconductor waveguide circuit using emitted photons," Phys. Rev. Lett. **110**, 037402 (2013).
23. D. G. Su'arez-Forero, M. J. Mehrabad, C. Vega, *et al.*, "Chiral quantum optics: recent developments, and future directions," arXiv (2024).
24. S. Barik, A. Karasahin, C. Flower, *et al.*, "A topological quantum optics interface," Science **359**, 666–668 (2018).
25. H. Siampour, C. O'Rourke, A. J. Brash, *et al.*, "Observation of large spontaneous emission rate enhancement of quantum dots in a broken-symmetry slow-light waveguide," npj Quantum Inf. **9**, 15 (2023).
26. N. J. Martin, D. Hallett, M. Duda, *et al.*, "Purcell-enhanced, directional light–matter interaction in a waveguide-coupled nanocavity," Optica **12**, 1100–1108 (2025).
27. D. L. Hurst, D. M. Price, C. Bentham, *et al.*, "Nonreciprocal transmission and reflection of a chirally coupled quantum dot," Nano Lett. **18**, 5475–5481 (2018).
28. M. J. R. Staunstrup, A. Tiranov, Y. Wang, *et al.*, "Direct observation of a few-photon phase shift induced by a single quantum emitter in a waveguide," Nat. Commun. **15**, 7583 (2024).
29. V. W. Scarola, K. Park, and S. D. Sarma, "Chirality in quantum computation with spin cluster qubits," Phys. Rev. Lett. **93**, 120503 (2004).
30. H. Pichler, T. Ramos, A. J. Daley, *et al.*, "Quantum optics of chiral spin networks," Phys. Rev. A **91**, 042116 (2015).
31. M. Reindl, J. H. Weber, D. Huber, *et al.*, "Highly indistinguishable single photons from incoherently excited quantum dots," Phys. Rev. B **100**, 155420 (2019).
32. P. Henzler, C. Traum, M. Holtkemper, *et al.*, "Femtosecond transfer and manipulation of persistent hot-trion coherence in a single CdSe/ZnSe quantum dot," Phys. Rev. Lett. **126**, 067402 (2021).
33. M. N. Makhonin, J. E. Dixon, R. J. Coles, *et al.*, "Waveguide coupled resonance fluorescence from on-chip quantum emitter," Nano Lett. **14**, 6997–7002 (2014).
34. A. Javadi, D. Ding, M. H. Appel, *et al.*, "Spin–photon interface and spin-controlled photon switching in a nanobeam waveguide," Nat. Nanotechnol. **13**, 398–403 (2018).
35. Y. Benny, S. Khatsevich, Y. Kodriano, *et al.*, "Coherent optical writing and reading of the exciton spin state in single quantum dots," Phys. Rev. Lett. **106**, 040504 (2011).
36. Y. Benny, Y. Kodriano, E. Poem, *et al.*, "Two-photon photoluminescence excitation spectroscopy of single quantum dots," Phys. Rev. B **84**, 075473 (2011).
37. Y. Benny, Y. Kodriano, E. Poem, *et al.*, "Excitation spectroscopy of single quantum dots at tunable positive, neutral, and negative charge states," Phys. Rev. B **86**, 085306 (2012).
38. D. Ding, M. H. Appel, A. Javadi, *et al.*, "Coherent optical control of a quantum-dot spin-qubit in a waveguide-based spin-photon interface," Phys. Rev. Appl **11**, 031002 (2019).
39. S. Stobbe, P. T. Kristensen, J. E. Mortensen, *et al.*, "Spontaneous emission from large quantum dots in nanostructures: exciton-photon interaction beyond the dipole approximation," Phys. Rev. B **86**, 085304 (2012).
40. P. Tighineanu, A. S. Sørensen, S. Stobbe, *et al.*, "Unraveling the mesoscopic character of quantum dots in nanophotonics," Phys. Rev. Lett. **114**, 247401 (2015).
41. J. Houel, A. V. Kuhlmann, L. Greuter, *et al.*, "Probing single-charge fluctuations at a GaAs/AlAs interface using laser spectroscopy on a nearby InGaAs quantum dot," Phys. Rev. Lett. **108**, 107401 (2012).
42. H. S. Nguyen, G. Sallen, C. Voisin, *et al.*, "Optically gated resonant emission of single quantum dots," Phys. Rev. Lett. **108**, 057401 (2012).
43. J. H. Quilter, A. J. Brash, F. Liu, *et al.*, "Phonon-assisted population inversion of a single InGaAs/GaAs quantum dot by pulsed laser excitation," Phys. Rev. Lett. **114**, 137401 (2015).
44. K. Boos, F. Sbresny, S. K. Kim, *et al.*, "Coherent swing-up excitation for semiconductor quantum dots," Adv. Quantum Technol. **7**, 2300359 (2024).